OPEN BIOLOGY

royalsocietypublishing.org/journal/rsob

Methods and techniques

Check for updates

Cite this article: Riquelme-Guzmán C, Beck T, Edwards-Jorquera S, Schlüßler R, Müller P, Guck J, Möllmert S, Sandoval-Guzmán T. 2022 *In vivo* assessment of mechanical properties during axolotl development and regeneration using confocal Brillouin microscopy. *Open Biol.* **12**: 220078.
https://doi.org/10.1098/rsob.220078

Received: 16 March 2022
Accepted: 31 May 2022

Subject Area:
developmental biology/biophysics/cellular biology

Keywords:
axolotl, confocal Brillouin microscopy, cartilage, development, regeneration

Authors for correspondence:
Stephanie Möllmert
e-mail: stephanie.moellmert@mpl.mpg.de
Tatiana Sandoval-Guzmán
e-mail: tatiana.sandoval_guzman@tu-dresden.de

†These authors contributed equally to this work.

THE ROYAL SOCIETY PUBLISHING

In vivo assessment of mechanical properties during axolotl development and regeneration using confocal Brillouin microscopy

Camilo Riquelme-Guzmán[1,3,†], Timon Beck[2,4,†], Sandra Edwards-Jorquera[3,†], Raimund Schlüßler[2], Paul Müller[2,4], Jochen Guck[2,4], Stephanie Möllmert[2,4] and Tatiana Sandoval-Guzmán[3,5]

[1]CRTD/Center for Regenerative Therapies TU Dresden, Center for Molecular and Cellular Bioengineering, Technische Universität Dresden, Dresden, Germany
[2]Biotechnology Center, Center for Molecular and Cellular Bioengineering, Technische Universität Dresden, Dresden, Germany
[3]Department of Internal Medicine 3, Center for Healthy Aging, University Hospital Carl Gustav Carus, Technische Universität Dresden, Dresden, Germany
[4]Max Planck Institute for the Science of Light and Max-Planck-Zentrum für Physik und Medizin, Erlangen, Germany
[5]Paul Langerhans Institute Dresden, Helmholtz Centre Munich, University Hospital Carl Gustav Carus, Technische Universität Dresden, Dresden, Germany

CR-G, 0000-0002-5126-6584; TB, 0000-0001-8529-5079; SE-J, 0000-0002-0519-4786; RS, 0000-0003-3752-2382; PM, 0000-0002-5734-3130; JG, 0000-0002-1453-6119; SM, 0000-0003-2121-9506; TS-G, 0000-0003-1802-5145

In processes such as development and regeneration, where large cellular and tissue rearrangements occur, cell fate and behaviour are strongly influenced by tissue mechanics. While most well-established tools probing mechanical properties require an invasive sample preparation, confocal Brillouin microscopy captures mechanical parameters optically with high resolution in a contact-free and label-free fashion. In this work, we took advantage of this tool and the transparency of the highly regenerative axolotl to probe its mechanical properties *in vivo* for the first time. We mapped the Brillouin frequency shift with high resolution in developing limbs and regenerating digits, the most studied structures in the axolotl. We detected a gradual increase in the cartilage Brillouin frequency shift, suggesting decreasing tissue compressibility during both development and regeneration. Moreover, we were able to correlate such an increase with the regeneration stage, which was undetected with fluorescence microscopy imaging. The present work evidences the potential of Brillouin microscopy to unravel the mechanical changes occurring *in vivo* in axolotls, setting the basis to apply this technique in the growing field of epimorphic regeneration.

1. Introduction

Regeneration is the ability to repair and regrow injured or lost body parts, allowing the re-establishment of the missing structure and its functionality. Although an advantageous feature in some multicellular organisms, the potential for regeneration has greatly diverged throughout evolution [1]. Among vertebrates, the most remarkable regeneration abilities are reported in urodele amphibians (salamanders and newts) as they are capable of restoring complex structures throughout their lives, such as the retina [2], heart [3], central nervous system [4] and appendages [5–7]. Conversely, regeneration abilities in mammals are mainly observed in organs and tissues, and in most cases, only a partial restoration of the structure and function is achieved after injury [8].

However, regeneration of complex structures have been reported in digit tips in mice [9] and human children [10].

Considering the remarkable regeneration abilities of urodeles, an extensive body of research has focused on understanding the process of limb regeneration and its regulation, with the ultimate goal of translating such knowledge into the development of regenerative therapies in humans [11]. Our knowledge on gene expression and cell transdifferentiation trajectories has advanced considerably in the recent years [12–17]; however, the influence of the extracellular environment and tissue mechanical properties has remained largely unexplored.

Cells sense and integrate mechanical cues that regulate their fate and behaviour [18,19]. Indeed, mechanical signals direct different stages of embryogenesis [20–23], cell fate during organogenesis [24–28] and loss of stemness during ageing [29,30]. Moreover, mechanical properties play key roles in pathological conditions such as fibrosis and cancer [31–33]. Comparatively, little is known about the role of tissue mechanics on animal regeneration. Considering the similarities to embryogenesis, particularly regarding large-scale tissue movements and patterning, it is very likely that physical forces and properties play an equally relevant role (reviewed in [34]). Therefore, complementing our cellular and molecular knowledge with biomechanical measurements will improve our understanding of limb regeneration.

A variety of techniques have been developed to quantify the mechanical properties of biological samples [35]. These methods, however, present some limitations that hinder their use for *in vivo* measurements, such as the need for direct contact with the cells of interest or rather poor three-dimensional and/or subcellular resolutions. To overcome such limitations, confocal Brillouin microscopy has emerged as a non-destructive, label-free and contact-free method that can probe viscoelastic properties of biological samples in three dimensions (reviewed in [36]). This technique is a type of optical elastography, originally developed in the context of material science, which became widely used for the study of condensed matter [37] and was combined with scanning confocal microscopy in the last decades for the measurement of biological samples [38]. Confocal Brillouin microscopy uses the inelastic scattering of light due to interactions between incident photons and spontaneous thermally induced density fluctuations, which can be described as a population of microscopic acoustic waves, called phonons. The scattering process causes an energy transfer between the phonons and the incident photons, which is detectable as a frequency difference between incident and scattered light (the Brillouin frequency shift). Importantly, the sound-wave properties exhibit an intrinsic dependence on the material's viscoelastic properties (i.e. the longitudinal modulus and the viscosity). The viscosity of the material will attenuate the propagation of the acoustic wave due to energy dissipation and is proportional to the linewidth of the Brillouin scattered light spectrum. The Brillouin frequency shift is proportional to the square root of the longitudinal modulus which describes a material's elastic deformability under a distinct type of mechanical loading (i.e. longitudinal compressibility). For sake of conciseness, we will use the term 'compressibility' instead of 'longitudinal compressibility' in the rest of the text (see 'Material and methods'). The Brillouin frequency shift furthermore depends on the sample's refractive index and density. Notably, it has been shown that changes in the Brillouin frequency shift typically arise from changes in the longitudinal modulus and that the influence of changes in refractive index and density may be negligible for samples with low lipid content [39–41].

Thus far, confocal Brillouin microscopy has been used for the measurements of viscoelastic parameters in the eye and cornea [42,43], cancer tumours and organoids [44,45], bone and cartilage [46–48], neurons and glia [39], among other tissues, using different animal models as well as human samples. In the context of regeneration, confocal Brillouin microscopy has recently been used to study spinal cord regeneration in the zebrafish [39] and bone regeneration in rabbits [47]. Whereas atomic force microscopy-based indentation measurements, the current gold standard in mechanobiology [49], have been more extensively used in the field [50–52], albeit with the limitation of measuring processed tissues from *ex vivo* explants. In urodeles, the only studies on tissue mechanics were performed either *in vitro*, demonstrating that wound closure of skin explants strongly relies on the substrate biomechanical properties [53], or *in silico*, predicting that movement-induced interstitial pressure promotes tissue growth during joint morphogenesis [54]. Hence, further *in vivo* studies need to be carried out to better understand the influence of mechanics on regeneration.

In this work, we measured for the first time the viscoelastic properties of a tetrapod limb *in vivo*. Using a confocal Brillouin microscope, we assessed the mechanical properties of the cartilaginous skeleton during development and regeneration of the axolotl (*Ambystoma mexicanum*). The cartilage is a prominent structure in the limb that is formed/regenerated by chondroprogenitors which produce a specialized extracellular matrix (ECM), giving the cartilage its characteristic mechanical properties [55]. Here, we provide evidence that disruption of cartilage integrity results in a sustained decrease of the Brillouin frequency shift values. In addition, we detected a continuous decrease in tissue compressibility during limb development and cartilage differentiation in the digit, revealed by increasing Brillouin frequency shift values. Furthermore, we quantitatively mapped the mechanical properties inside the developing limbs and digits of live animals and were able to identify several anatomical structures, such as different stages of cartilage condensation, interstitial space and epidermis. Finally, we followed regeneration *in vivo*, demonstrating changes in the mechanical properties of the cartilage at different time points after amputation. Specifically, we detected an initial decrease in Brillouin frequency shift values in early stages of regeneration, which later increased approaching the levels of intact digits.

This work constitutes the first step for the application of Brillouin microscopy as a mean to characterize the mechanical properties in the highly regenerative axolotl. Taking advantage of this animal model, future *in vivo* studies will certainly open new possibilities to further comprehend the complexity of the regenerative process.

2. Material and methods

2.1. Animal husbandry and handling

Husbandry and experimental procedures were performed according to the Animal Ethics Committee of the State of Saxony, Germany. Axolotls were kept and bred in the axolotl facility of the Center for Regenerative Therapies Dresden

Table 1. Transgenic reporter lines.

short name	complete genotype	reference
CAGGs:GFP	TgScel*(CAGGs:eGFP)*^{ETNKA}	[57]
Sox9-mCherry	C-Ti$^{t/+}$*(Sox9:Sox9-T2a-mCherry)*^{ETNKA}	[56]

(CRTD) of the Technische Universität Dresden (TUD). A full description of the husbandry conditions was recently published [56].

Animals were selected by their snout to tail length (ST), which is indicated individually in each experiment. The transgenic reporter lines are indicated in table 1.

The *CAGGs:GFP* line expresses *eGFP* driven by a modified cytomegalovirus-immediate early promoter, a strong and constitutively active promoter. Thus, eGFP is expressed in all cells [57]. The *Sox9-mCherry* line has the mCherry protein fused to the endogenous SOX9 protein via a T2a self-cleaving peptide. Therefore, mCherry is present in all SOX9$^+$ cells, which are particularly abundant in the cartilage [56].

Prior to all procedures, animals were anaesthetized with 0.01% benzocaine solution diluted in tap water. After collection of tissues or when experiment was finished, animals were euthanized by exposing them to lethal anaesthesia (0.1% benzocaine) for at least 20 min. Further experimental details are described in each case specifically.

2.2. Confocal Brillouin microscopy and data analysis

Brillouin maps were acquired using a custom-built confocal Brillouin microscope previously described [39]. The set-up is based on a two-stage VIPA interferometer. Illumination was achieved by a frequency-modulated diode laser with a wavelength of 780.24 nm. The laser frequency was stabilized to the D2 transition of rubidium 85. The set-up has a CMOS camera (IDS UI-1492LE-M), which allows widefield images to be taken. Image acquisition was done with the custom-made software BrillouinAcquisition (BrillouinAcquisition v. 0.2.2: C++ program for the acquisition of FOB microscopy datasets, available at https://github.com/BrillouinMicroscopy/BrillouinAcquisition). Imaging was performed using a Zeiss Plan Neofluar 20 x/0.5 objective, resulting in a spatial optical resolution of 1 µm in the lateral plane and 5 µm in the axial direction. The area of the imaged region and pixel size are indicated individually in each experiment.

Acquired data were analysed using the custom-made software BrillouinEvaluation (BrillouinEvaluation v. 1.5.3: Matlab program for the evaluation of Brillouin microscopy datasets, available at https://github.com/BrillouinMicroscopy/BrillouinEvaluation), and values in each map were exported to a CSV file. To analyse discrete areas within our Brillouin frequency shift maps, the custom-made software Impose was used (Impose v. 0.1.2: Graphical user interface for superimposing and quantifying data from different imaging modalities, available at https://github.com/GuckLab/impose).

The measured Brillouin frequency shift ν_B can be expressed in terms of the longitudinal Modulus M', refractive index n and density of the specimen, as well as the incident wavelength λ_0 and scattering angle θ given by the set-up: $\nu_B = \frac{2n\sqrt{M'}}{\lambda_0\sqrt{\rho}}\sin(\theta/2)$. All measurements were performed in a backscattering configuration with $\theta = 180°$ and accordingly $\sin(\theta/2) = 1$. The longitudinal compressibility κ_L may be expressed as the inverse of the longitudinal modulus: $\kappa_L = 1/M'$. For the sake of conciseness κ_L will be called 'compressibility' in the rest of the text, despite the fact that this term is usually defined as the inverse of the bulk modulus K'. Bulk modulus K' and longitudinal modulus M' are related by the following equation in case of an isotropic sample: $M' = K' + \frac{4}{3}G'$.

To facilitate the comparison with the results of other Brillouin microscopes, we normalized the measured Brillouin frequency shift ν_B values with the Brillouin frequency shift of water $\nu_B^{water} = 5.066$ GHz. The dimensionless *Brillouin elastic contrast* $\overline{\nu_B}$ was previously introduced according to the following formula: $\overline{\nu_B} = (\nu_B/\nu_B^{water}) - 1$ [58]. $\overline{\nu_B}$ carries the same information as the Brillouin frequency shift ν_B, but does not depend on the incident wavelength λ_0.

2.3. Imaging cartilage mechanical properties upon collagenase treatment *ex vivo*

For *ex vivo* measurements, we used the *CAGGs:GFP* reporter line (5–8 cm ST). One hand was collected and imaged immediately (no treatment) by placing it on a glass-bottomed dish (Ø: 50/40 mm, Willco Wells HBSB-5040) with a silica block laid on top to flatten it and improve light penetrance. To properly place the focus in the region of interest (ROI) (proximal resting zone (RZ) in distal phalanx of second digit), we used the fluorescence signal from our transgenic line and acquired a widefield image. After Brillouin image acquisition, hands were incubated with Liberase (0.35 mg ml^{-1} in 80% PBS, Sigma LIBTM-RO) for 30 min in a thermal mixer at 37°C. Next, hands were rinsed briefly with 80% PBS and imaged again following the same steps mentioned before. A second incubation with the collagenase mix was performed for 15 min (45 min in total) prior to final imaging with the confocal Brillouin microscope. Generated maps correspond to a region of 148 × 80 µm, using a pixel size of 2 µm, averaging two acquisitions of 0.5 s per pixel.

2.4. Imaging mechanical properties during digit development *in vivo*

To follow the development of the digit, we used the *Sox9-mCherry* line and selected larvae at developmental stages 45, 47, 49, 51 and 53, based on morphological parameters and mCherry expression pattern, as previously described [59,60]. Animals were anaesthetized and later immobilized on top of glass-bottomed dishes. They were mounted laterally to ensure proximity between the developing limb and the glass. Images were acquired with the Brillouin confocal microscope using a 5 µm step size and 0.5 s acquisition time. The size of the Brillouin map was not constant, as animals grow fast during early phases of development [56]. Thus, the acquisition area was defined according to the size of the structure of interest.

After imaging, animals were euthanized and fixed with MEMFa (MOPS 0.1 M pH 7.4, EGTA 2 mM, $MgSO_4$-$7H_2O$ 1 mM, 3.7% formaldehyde) overnight at 4°C, washed with PBS and delipidated with a solution containing sodium dodecyl sulfate 4% and boric acid 200 mM, pH 8.5, on a

rocker at 37°C for 20 min. Next, the embryos were washed with PBS and stained with Hoechst 33342 (1 : 2000 in PBS, Invitrogen H3570) for 1 h, after which embryos were cleared by an overnight wash at room temperature with a refractive index matching solution (EasyIndex RI 1.52). Cleared embryos were mounted in the same way as for Brillouin imaging and were imaged on an inverted Zeiss confocal laser scanning microscope LSM780 using a Plan-apochromat 10 x/0.45 objective. Non-cleared embryos were imaged at stages 51 and 53 under the same microscope to reveal anatomical structures in developing digits.

2.5. Imaging mechanical properties during digit regeneration *in vivo*

For digit regeneration experiments, we used the *Sox9-mCherry* line (4 cm ST). Animals were anaesthetized and imaged by placing them on top of glass-bottomed dishes. The hand was positioned properly prior to be flattened and immobilized. A wet tissue with benzocaine was placed on top of animals during imaging to prevent them from drying. After measurements with the Brillouin confocal microscope, animals were imaged *in vivo* with an inverted Zeiss confocal laser scanning microscope LSM780 (Plan-apochromat 20 x/0.8) to reveal the mCherry^{+} cartilage. Imaging with both microscopes was performed before, at 15- and 30-day post-amputation (0, 15 and 30 dpa, respectively).

Amputation was performed at the joint of the distal phalanx in the second digit. After the surgical procedure, the animals were covered with a wet tissue (with benzocaine) and allowed to recover for 10 min, before transferring them back to holding water.

Generated maps correspond to a 200 × 80 µm region, using a 2.5 µm step size, averaging 2 acquisitions of 0.5 s *per* pixel. To correlate our Brillouin maps with regeneration progress, we used *Sox9-mCherry* siblings that were amputated within the same day as the ones used for Brillouin imaging. Animals were imaged with an Olympus SZX10 stereoscope, using the Olympus cellSens Entry software. We measured the length of the digits from the joint to their distal-most tip and normalized their length with respect to day 0 (both for regenerating as well as undamaged digits).

2.6. Brillouin data representation and statistical analysis

All graphs and all Brillouin maps were generated by graphing the exported data as heat maps with GraphPad Prism software. To calculate the average Brillouin elastic contrast within a defined ROI, the values were extracted from the Brillouin maps, averaged per animal and plotted for multiple comparisons. To generate the linear signal distribution graphs during development (figure 3*f*), five consecutive transversal lines were drawn in each Brillouin elastic contrast map acquired for developing limb buds or digits. In all cases, drawn lines had a width of 1 µm and were separated by 5 µm between them. Brillouin elastic contrast values were extracted from each line and averaged, generating one line per sample. Considering the differing sizes of limb buds and digits during development, structure size was normalized, with its centre set as point zero and both edges as ±100%. Edges were defined by Brillouin elastic contrast values below 0.006 (equivalent to benzocaine solution). Values from one representative individual *per* developmental stage were plotted together for qualitative comparison of changes occurring during development.

Images obtained with the confocal microscope or the wide-field set-up of the Brillouin microscope were processed with the open source software Fiji (https://imagej.net/software/fiji/) [61]. The images from developing limbs/digits correspond to a maximum intensity Z-stack projection. The Hoechst-derived nuclear signal was used to generate a mask to show the outline of the developing limbs/hands, which is displayed together with the mCherry signal, revealing *Sox9* expressing cells. The images of regenerating digits correspond to a maximum intensity Z-stack projection of four optical planes (1 µm interval), which correlates to the thickness of the section measured with the Brillouin confocal microscope [39].

Statistical analysis was carried out using Origin Lab Pro 2021b. N_A refers to the number of animals. N_C refers to the number of cells. All data were subjected to normality tests using the Chen–Shapiro test. If normality couldn't be rejected, statistical analysis proceeded with a *t*-test (figure 1*d*, $N_C = 20$). Since almost all normality test methods perform poorly for small sample sizes (less than or equal to 30), and Chen–Shapiro test results additionally yielded too few data points to assume normal distributions, we proceed with non-parametric statistical tests for all other analyses. In particular, the data in figure 2*d* ($N_A = 5$) comprises three repeated measures of the same specimens, which requires the Friedman ANOVA. The test yields a test statistic $\chi_2{}^2 = 10$ with a probability $p = 0.00674$. *Post hoc* analysis with Dunn's test revealed a significant statistical difference between '0 min' and '45 min' ($p = 0.0047$), but not between any other pairings. The effect size was determined using Kendall's W test with $W = \frac{X^2}{N_A(k-1)}$, where X^2 is the Friedman test statistic value, N_A is the sample size, k is the number of measurements *per* subject [62]. In our case $W = 1$ (large effect). The data in figure 3*g* ($N_A \geq 4$) comprises independent samples. Here, we employed the Kruskal–Wallis ANOVA which yielded a test statistic $\chi_4{}^2 = 15.21273$ with a probability $p = 0.00428$. Dunn's *post hoc* analysis revealed a statistically significant difference between developmental stage '45' and '53' ($p = 0.01411$) and developmental stage '47' and '53' ($p = 0.02106$), but not any of the other pairings. The Kruskal–Wallis effect size η^2 was calculated using $\eta^2 = \frac{X^2 - k + 1}{N - k}$, where χ^2 is the Kruskal–Wallis test statistic value; k is the number of groups and N is the total number of observations [62]. In our case $\eta^2 = 0.62$ (large effect). The data in figure 4*c* ($N_A = 4$) comprises repeated measures of the same digits and animals. However, the pairwise difference between the amputated and the contralateral digit was of interest, not the difference of the repeated measurements. Therefore, we used the Mann–Whitney test which yields a test statistic $U = 0$ with a Z score = −2.16506 and a probability $p = 0.02857$ for each pairwise comparison of amputated and contralateral digits at 15 dpa and 30 dpa. The effect size r was calculated using $r = |Z|/\sqrt{N_A}$ and $r = 0.76$ (large effect) for both time points. The data in figure 4*e* comprises repeated measures of the same animals. The Friedman ANOVA yields a test statistic $\chi_2{}^2 = 6.5$ with a probability $p = 0.03877$. *Post hoc* analysis with Dunn's test revealed a significant statistical difference between '0 dpa' and '15 dpa' ($p = 0.03998$), but not between any other pairings. The effect size $W = 0.81$ (large effect).

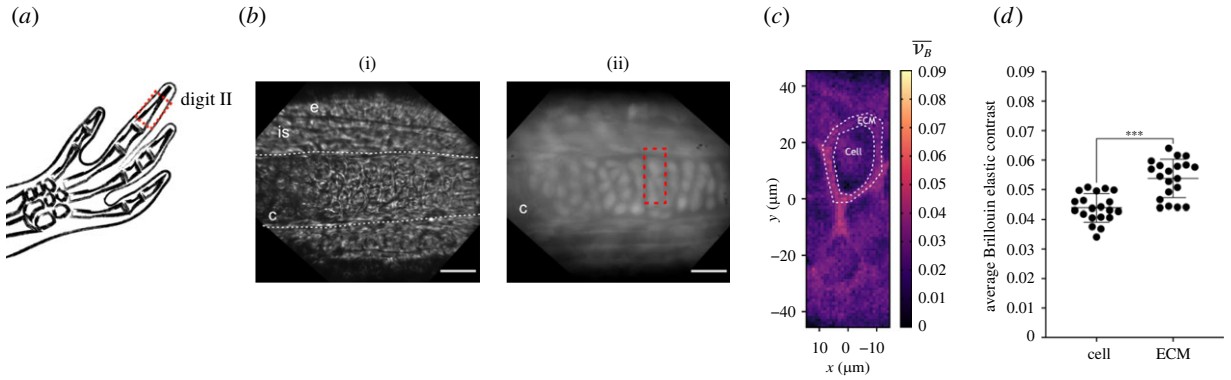

Figure 1. Confocal Brillouin microscopy maps cartilage architecture, identifying differences between chondrocytes and ECM (*a*) Schematic representation of the distal phalanx in digit II, generated with Keynote. The red rectangle indicates the imaged area, shown in (*b*). (*b*)(i) Brightfield image of probed region. Dashed lines show the position of the phalanx. (ii) Widefield fluorescence image using *CAGGs:GFP* reporter line. All cells were eGFP$^+$. Red rectangle shows region probed with the Brillouin microscope shown in (*c*). c, cartilage; e, epidermis; is, interstitial space. Scale bar: 50 µm. (*c*) Brillouin elastic contrast ($\overline{\nu_B}$) maps for the region shown in (*b*). The Brillouin elastic contract (normalized Brillouin frequency shift) is indicative of the elastic properties. Dashed oval shows segmented cell as an example of quantifications shown in (*d*). (*d*) Quantification of average Brillouin elastic contrast inside cells (chondrocytes) and the surrounding ECM. $N_C = 20$, $N_A = 4$, *t*-test, *** $p < 0.001$.

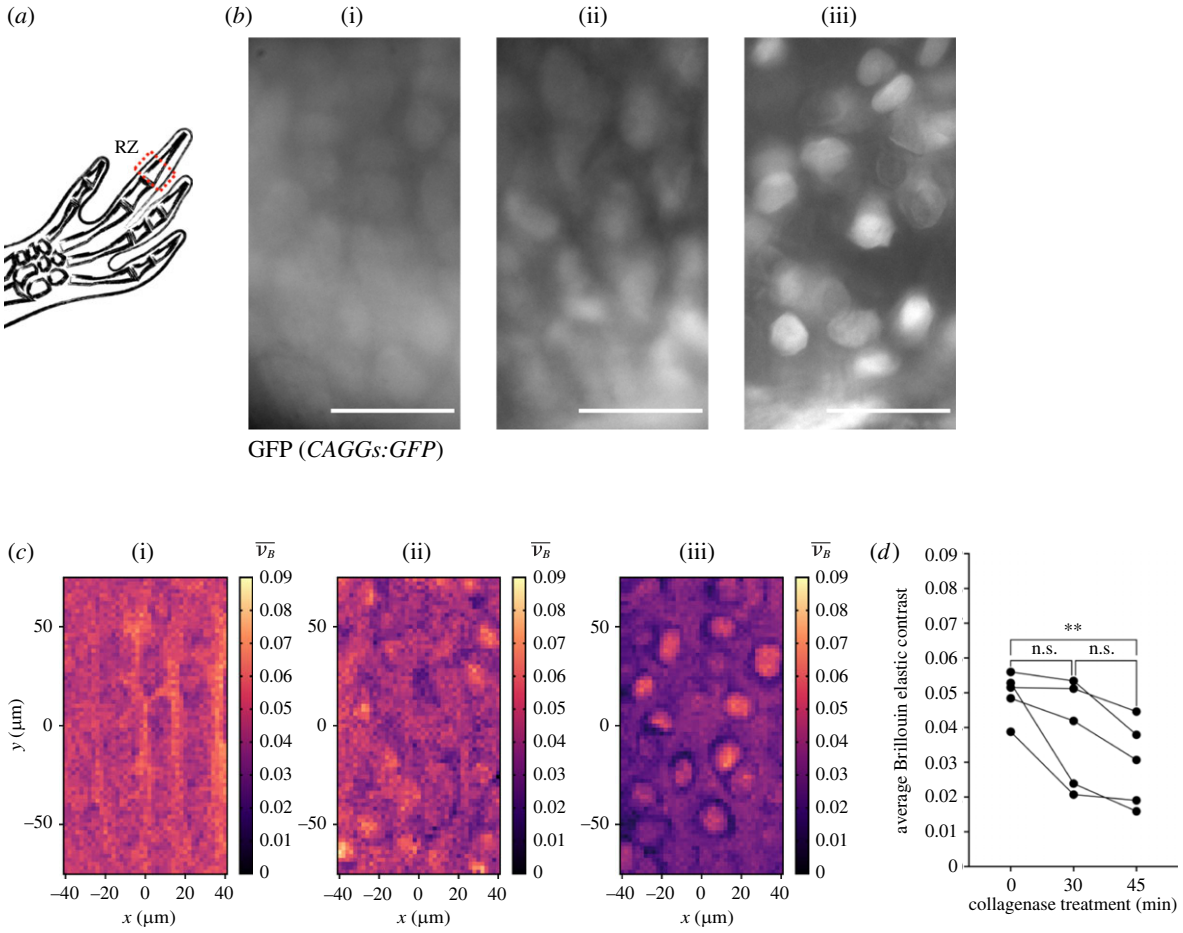

Figure 2. Loss of tissue integrity assessment with confocal Brillouin microscopy. (*a*) Schematic representation of proximal RZ of the distal phalanx in digit II, generated with Keynote. (*b*) Widefield fluorescence images of region in *CAGGs:GFP* hands treated with collagenase at different times, which were probed using confocal Brillouin microscopy. (i) No treatment, (ii) 30 min, (iii) 45 min. Scale bar: 50 µm. (*c*) Brillouin elastic contrast ($\overline{\nu_B}$) maps for the regions shown in (*b*). (i) No treatment, (ii) 30 min, (iii) 45 min. Maps reveal a time-dependent loss of tissue integrity upon collagenase treatment. (*d*) Average $\overline{\nu_B}$ values of maps generated from *CAGGs:GFP* hands treated with collagenase. $N_A = 5$, Friedman ANOVA with Dunn's *post hoc* analysis, **$p < 0.01$.

3. Results

3.1. Confocal Brillouin microscopy maps cartilage architecture, identifying differences between chondrocytes and extracellular matrix

In vivo experiments in the axolotl are largely possible thanks to its transparency, particularly during juvenile stages, allowing the study of regeneration dynamics by using a diverse array of microscopy techniques. To evaluate how efficiently the mechanical properties in axolotl tissues can be probed, we tested the cartilaginous phalanxes using a confocal Brillouin microscope (figure 1*a*). Structurally, the cartilage is a tissue devoid of blood vessels and nerves, formed by chondrocytes embedded in a dense ECM, which contains in its majority collagen and, to a lesser extent, proteoglycans [63]. In juvenile axolotls, appendicular skeleton is

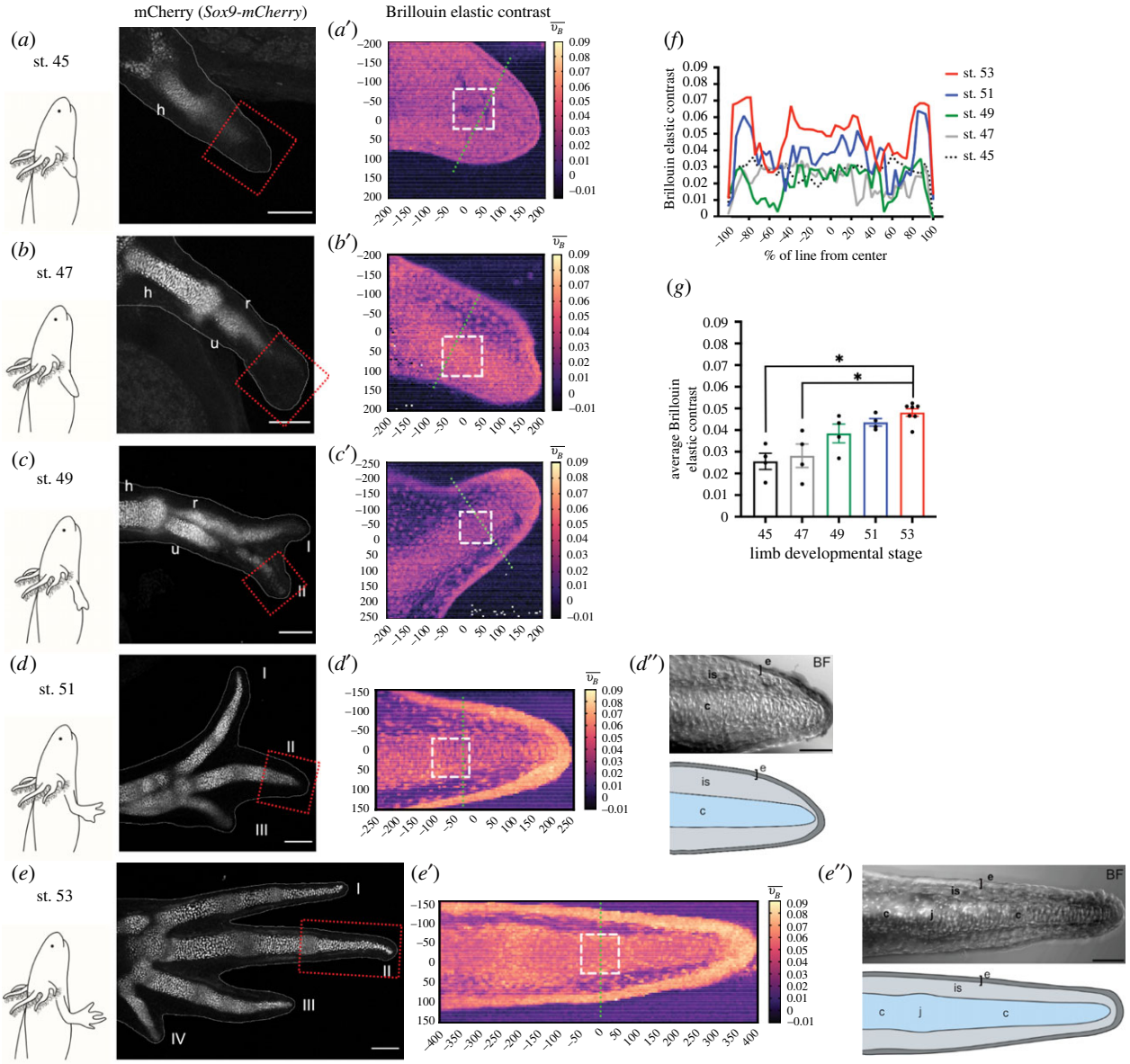

Figure 3. The Brillouin elastic contrast increases progressively during digit development. (*a–e*) Left: schematic representation of limb development stages (45, 47, 49, 51, 53), generated with BioRender.com. Right: Confocal imaging of cleared *Sox9-mCherry* transgenic animals after Brillouin acquisition for each developmental stage. White dashed lines show limbs outline derived from nuclear staining with Hoechst. The red square represents the region probed with the Brillouin microscope. h: humerus, u: ulna, r: radius, I–IV: digit I–IV. Scale bar: 200 µm. (*a′–e′*) Brillouin elastic contrast ($\overline{\nu_B}$) maps for regions shown in (*a–e*). Green dashed lines represent zones quantified in (*f*). White squares represent regions quantified in (*g*). Different structures in the digit were identified by their differences in the Brillouin frequency shift values. (*d″–e″*) Top: Brightfield images of digit II (BF) from developmental stages 51 and 53. Scale bar: 100 µm. Bottom: Schematic representation of digit II with delineated tissue types. c, cartilage; e, epidermis; is, interstitial space; j, joint. Generated with BioRender.com. (*f*) Average $\overline{\nu_B}$ linear distribution along five transversal lines across the limb bud or digit II at different developmental stages ($N_A = 1$ representative animal/developmental stage). (*g*) Average $\overline{\nu_B}$ values of regions shown in white squares in (*a′–e′*). $N_A \geq 4$ animals/developmental stage, Kruskal–Wallis ANOVA with Dunn's *post hoc* analysis, $^*p < 0.05$.

cartilaginous [56] and this cartilage accounts for up to 50% of the exposed surface upon amputation [64].

To facilitate imaging the cartilage, we used *CAGGs:GFP* transgenic animals. This line expresses *eGFP* constitutively in all cells, allowing us to morphologically distinguish different tissues and structures (figure 1*b*). Particularly, the phalanx is an elongated structure with oval-shaped cells distributed along it (i.e. chondrocytes). Using 4 cm animals and a wide-field set-up, we could properly position the focus in a ROI (figure 1*b*, red rectangle) where the mechanical properties were assessed using the confocal Brillouin microscope. As shown in figure 1*c*, we successfully mapped the Brillouin elastic contrast ($\overline{\nu_B}$) of a region inside the digit cartilage. The Brillouin elastic contrast (i.e. normalized Brillouin frequency shift) is indicative of the elastic properties of the sample. In the generated maps, we identified chondrocytes by morphology, with lower values than the surrounding ECM. In agreement with former reports [65], our results suggest that the collagen-rich matrix is less compressible as compared to chondrocytes. Moreover, by creating a mask to independently quantify the Brillouin elastic contrast of cells and the ECM, we found that indeed the ECM had significantly higher values than the chondrocytes embedded within (figure 1*d*).

Altogether, we were able to successfully probe the mechanical properties of the cartilage in axolotl digits, providing sufficiently high resolution to distinguish differences between intracellular and extracellular environments.

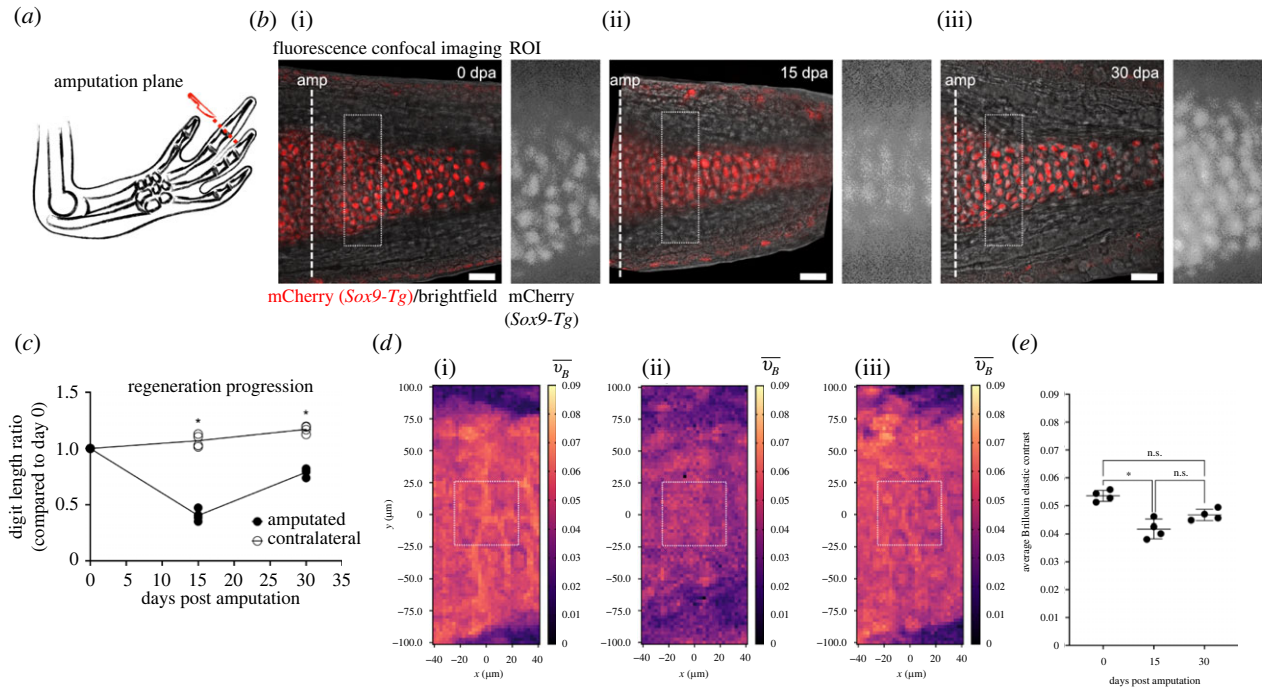

Figure 4. Brillouin elastic contrast increases as cartilage condensates during digit regeneration. (*a*) Schematic representation of amputation plane at the joint of the distal phalanx, generated with Keynote. (*b*) Confocal live imaging of digit II from *Sox9-mCherry* axolotl (i) before amputation (0 days post-amputation, dpa), and at (ii) 15 dpa and (iii) 30 dpa. Images represent a composite between brightfield and maximum intensity Z-stack projection of four optical slices for the mCherry signal. Dashed line at 0 dpa shows the amputation plane (amp). Dashed rectangles show ROI which was probed with the confocal Brillouin microscope. A widefield fluorescence image taken with Brillouin set-up of the ROI is shown to the right of each timepoint. Scale bar: 50 µm. (*c*) Regeneration progression as shown by the digit length ratio at each time point. (i) 0 dpa, (ii) 15 dpa, (iii) 30 dpa. Ratio was calculated comparing each digit length with respect to day 0. Line is connecting mean values. $N_A = 4$, Mann–Whitney test, $^*p < 0.05$, amputated versus contralateral. (*d*) Brillouin elastic contrast ($\overline{\nu_B}$) maps for ROIs shown in (*b*). White squares represent the region quantified in (*e*). Changes in $\overline{\nu_B}$ values were observed inside the cartilage at different timepoints. (*e*) Average $\overline{\nu_B}$ in cartilage during regeneration. $N_A = 4$, Friedman ANOVA with Dunn's *post hoc* analysis, $^*p < 0.05$.

3.2. Confocal Brillouin microscopy is sensitive to changes in cartilage architecture

Having demonstrated that the cartilage architecture can be mapped with confocal Brillouin microscopy, we wondered if changes in tissue structure could be assessed with this technique as well. We thus developed a protocol to follow the loss of tissue integrity via enzymatic treatment. As most of the ECM in cartilage is made of collagen, we treated the tissue with a protease mix enriched in collagenases (Liberase). We collected hands from 5 to 8 cm *CAGGs:GFP* animals and incubated them with the collagenase mix for 30 and 45 min at 37°C. For imaging, we always selected the proximal resting zone (RZ) of the distal phalanx in the second digit (figure 2*a*). The RZ corresponds to a region in which rounded quiescent chondrocytes are found at both ends of the skeletal element. As observed in the fluorescent microscopy images, treatment with collagenase did not largely affect the organization of chondrocytes at 30 min, but at 45 min a higher disruption of the tissue was observed, together with a reduction in cell density (figure 2*b*). Noteworthy, positioning the sample in the RZ was still possible, as the overall structure of the phalanx remained distinguishable.

Using the confocal Brillouin microscope, we imaged a 148 × 80 µm region with a pixel size of 2 µm in the RZ (figure 2*c*). The Brillouin elastic contrast map in the RZ for untreated samples was similar to the one in figure 1*c*, with higher values in the ECM compared to the chondrocytes. Upon treatment for 30 min, a decrease in the Brillouin elastic contrast was seen throughout the sample, particularly in the ECM. At 45 min, the values in the ECM were further decreased, allowing the cells to be easily visible in the map. Interestingly, the chondrocytes seemed to round up after the protease treatment (figure 2*b*), accompanied by an increase of their Brillouin elastic contrast values. A similar phenomenon has been shown to occur in mesenchymal stem cells, as they stiffen immediately after detachment [66].

To quantitatively compare the changes in the mechanical properties during the enzymatic treatment, we quantified the Brillouin elastic contrast in the whole region by averaging all pixels in the map (figure 2*d*). Congruent with our qualitative observations, we detected a significant reduction in the Brillouin elastic contrast values after 45 min of enzymatic treatment. Overall, using the Brillouin microscope, we were able to spatially map the changes in the tissue architecture and mechanical properties of axolotl cartilage *ex vivo* upon protease treatment, as well as quantifying the increase in tissue compressibility during its loss of integrity.

3.3. The Brillouin elastic contrast increases progressively during digit development

To assess the physiological mechanical changes in the axolotl, we imaged the formation of the digit at different developmental stages *in vivo*. Using the *Sox9-mCherry* transgenic line, we have shown mCherry+ cells to be found in all the cartilage [56].

We collected embryos at stages 45, 47, 49, 51 and 53 based on previous work [59,60]. Embryos were imaged with the confocal Brillouin microscope and subsequently collected, fixed and cleared in order to perform confocal imaging of the mCherry$^+$ region. At stage 45, no zeugopod is formed, and only a condensation of the humerus was observed (figure 3*a*). The zeugopod was observed at stage 47, when condensation of the radius and ulna became evident (figure 3*b*). From stage 49 onwards, condensation of the autopod skeletal elements were detected. Digits I and II were observed at stage 49 (figure 3*c*), followed by digit III at stage 51 (figure 3*d*) and digit IV at stage 53 (figure 3*e*). We measured with the confocal Brillouin microscope (pixel size 5 µm) in the distal-most part of the limb bud (stages 45 and 47) and, when the digits formed, in the distal end of digit II (figure 3*a–e*, red squares) assessing the change in mechanical properties during development.

At stage 45, the limb bud is a semi-homogeneous structure with practically no perceivable differences revealed by the Brillouin elastic contrast map (figure 3*a*′), although a thin layer at the edge of the limb bud could be distinguished, likely corresponding to its epithelium. At stage 47, the map showed a slight increase in Brillouin elastic contrast values in the middle region of the developing limb (figure 3*b*′). This increase could point towards early steps of cartilage condensation, which was not detected with the reporter of SOX9 expression (mCherry$^+$ cells). In stages 49, 51 and 53, the digit II was morphologically identified at different developmental stages using mCherry expression. Our results show that the Brillouin elastic contrast values progressively increased in the phalanx, as well as in the epidermis, during digit development (figure 3*c*′–*e*′), suggesting a decrease in tissue compressibility. Moreover, the Brillouin elastic contrast maps allowed us to recognize other structures such as the epidermis (outer layer) in all stages, which clearly thickens from stages 49 to 53, as well as the interstitial space (between the cartilage and epidermis), with likely some cells scattered throughout the tissue. Brightfield images of digit II at stages 51 and 53 reveal the digit anatomy during development, with a clear distinction between cartilage, epithelium and interstitial space (figure 3*d*″–*e*″). Furthermore, the Brillouin elastic contrast map at stage 53 reveals the location of the joint, with a subtle thickening of the skeletal element and slight increase in Brillouin elastic contrast values (between −250 and −150 µm in the *x*-axis; figure 3*e*′), which correlates with the joint location 500–600 µm from the digit tip, identified with brightfield imaging (figure 3*e*″).

Interestingly, we observed in developing digits that Brillouin elastic contrast values were higher in chondrocytes when compared to their surrounding ECM (figure 3*c*′–*e*′). This contrasts with what we observed in larger animals, where the ECM presented higher values than the chondrocytes embedded within (figures 1 and 2). This might be explained by development-associated changes in the cartilage matrix composition and deposition, which leads to progressively decreasing ECM compressibility (reviewed in [67]).

To further evaluate the mechanical differences within the limb bud and digit, we quantified the signal along several transversal lines (figure 3*a*′–*e*′, green dashed line) for every generated Brillouin elastic contrast map ($N_A = 5$). From these lines, we generated an average for each developmental stage (figure 3*f*). We observed a progressive increase in the average signal distribution with development. Moreover, this unidimensional data representation reveals the structures identified in our maps from stage 49 onwards (i.e. phalanx, interstitial space and epidermis) by their differences in the Brillouin elastic contrast.

Finally, to quantitatively assess the differences in the Brillouin elastic contrast during cartilage development, the signal within a 100 × 100 µm square region was averaged *per* animal (figure 3*a*′–*e*′, white dashed square). The regions selected correspond to mCherry$^+$ tissue of digit II or to the distal end of the limb bud in stages 45 and 47 as controls (figure 3*g*). As expected, a progressive increase in the Brillouin elastic contrast was observed in each developmental stage, suggesting a gradual decrease of cartilage compressibility. This observation is likely correlated with the increased ECM deposition and cell density that naturally occur during cartilage development [67].

Taken together, these results demonstrate the power of the confocal Brillouin microscope to probe mechanical properties in the axolotl *in vivo*. We were able to characterize the development of complex structures such as the digit, and to detect changes in tissue mechanics that were not measurable by the mere expression of transgenes.

3.4. Brillouin elastic contrast increases as cartilage condensates during digit regeneration

Considering our results hitherto, we next assessed if the confocal Brillouin microscope could also resolve mechanical changes occurring during regeneration. Thus, we acquired Brillouin elastic contrast maps of the cartilage during digit regeneration *in vivo*. For this, we amputated at the joint of the distal phalanx from the second digit in 4 cm axolotls (figure 4*a*). Using the *Sox9-mCherry* line, we were able to properly position the sample and thus image the condensation of the regenerating cartilage. After every measurement with the confocal Brillouin microscope, we performed live confocal fluorescence imaging in order to observe the morphology of the regenerating digit at the same optical plane (figure 4*b*). Before amputation (0 dpa), we observed the RZ of the mature phalanx which was located distal to the amputation plane. This zone corresponded to well-organized rounded chondrocytes. At 15 dpa, condensation had already started, evidenced by characteristic tightly packed mCherry$^+$ cells, forming an elongated structure. Finally, at 30 dpa, regeneration was in its later stages. A clearly defined digit was observed and the mCherry$^+$ cells presented a morphology resembling that of rounded chondrocytes from a mature digit (i.e. 0 dpa).

To quantify the general regeneration progress, we measured the length of the digit at these three time points and compared them to the contralateral one, i.e. the undamaged digit II of the opposite hand (figure 4*c*). A clear increase in the digit length was observed, which correlated with the progression of the regenerative process. Of note, even at 30 dpa, the length of the regenerated digit was significantly shorter than the contralateral one, indicating that the digit was not fully regenerated yet.

To compare the mechanical properties of the cartilage at these three different time points during regeneration, we measured the Brillouin elastic contrast in the mCherry$^+$ regions distal to the amputation plane (figure 4*b*, dashed rectangle). Similar to the abovementioned experiments, we were able to properly position the focus of the confocal Brillouin microscope using the mCherry signal and thus generate a Brillouin elastic contrast map covering mostly the cartilaginous tissue. The image corresponding to the acquired ROI was also used

to identify the correct imaging plane in the confocal fluorescence microscope.

By creating a 200 × 80 µm map with a 2.5 µm pixel size, we were able to properly distinguish the differences of the mechanical properties of the cartilage during regeneration (figure 4*d*). At 0 dpa, the ECM had a higher Brillouin elastic contrast than the chondrocytes within, and the interstitial tissue had lower values than the phalanx. These observations were in agreement with our observations in intact mature digits in previous sections. At 15 dpa, the Brillouin elastic contrast was importantly reduced, with no clear distinction between the ECM and the chondrocytes, albeit the cartilage could still be identified by presenting slightly higher values than the interstitial tissue. This observation might be due to the stage of differentiation, as the condensation of the cartilage at this time point was in its earliest steps. Finally, at 30 dpa, we observed a re-establishment of the mechanical properties in the phalanx, with a clear increase in the Brillouin elastic contrast in the cartilage, evidenced by the colour scale in the map. This map showed a similar trend to the uninjured digit, in which the ECM presented higher values than the cells embedded within.

To quantitatively assess the differences in the mechanical properties, we selected a 25 × 25 µm region in the centre of each phalanx (figure 4*d*, white squares) and averaged the values of all pixels within one region *per* animal (figure 4*e*). Congruent with our observations, we quantified a significant reduction in the Brillouin elastic contrast at 15 dpa compared to day 0, which suggests that the cartilage might be more compressible during the early stages of condensation in the regenerating digit. When we analysed the values at 30 dpa, we did not detect any significant difference with respect to either 0 or 15 dpa, suggesting that the tissue was in a transitioning stage, not yet reaching its final maturation. Thus, we could speculate that at later time points, the average Brillouin elastic contrast would reach equivalent values to the ones acquired in uninjured tissues. These observations contrast with the interpretation of our images obtained with confocal fluorescence imaging that suggested a re-establishment of the digit morphology after 30 days of regeneration (figure 4*b*, 30 dpa), thus revealing the strong capacity of Brillouin imaging for the detection of changes in viscoelastic tissue properties, which may be overlooked with traditional imaging techniques.

Collectively, our results provide novel evidence for the measurement of viscoelastic properties in the axolotl *in vivo*. We demonstrated how the tissue architecture can be described through mechanical parameters such as compressibility, represented by the Brillouin elastic contrast. Additionally, we have shown that the loss of tissue integrity can be detected through a change in tissue architecture, as well as an overall decreased Brillouin elastic contrast. We have also demonstrated for the first time that the tissues display increasingly reduced compressibility during the development of limbs and digits *in vivo*. Furthermore, using the confocal Brillouin microscope, we were able to distinguish differences in the mechanical properties of the cartilage during digit regeneration at different timepoints.

4. Discussion

In recent years, confocal Brillouin microscopy has emerged as a powerful label-free and contact-free tool to probe mechanical properties of biological samples (reviewed in [36]). Measurements of diverse systems have been carried out *in vitro* and *ex vivo*; however, the adaptation of confocal Brillouin microscopy for *in vivo* animal models has only been performed using zebrafish larvae to study spinal cord repair and growth [39], the material properties in the notochord [65] and retina development [68]. In this report, we present for the first time an assessment of the *in vivo* mechanical properties of the axolotl, both during development and regeneration. Thereby, we add to the existing literature by providing yet another application of Brillouin microscopy to the field of tissue mechanics.

The composition and structure of the ECM entails tissue-specific biochemical and biomechanical properties that play key roles in homeostasis and pathologies, such as cancer and fibrotic disorders (reviewed in [69]). In addition, due to the pronounced contribution of the ECM to mechanical tissue properties, the ECM and its constituents have been targeted in various experiments employing Brillouin light scattering [70–73]. This also includes studies on the ECM-rich cartilage tissue, in which an important reduction of the Brillouin frequency shift was reported in porcine articular cartilage treated with trypsin, due to degradation of proteoglycans [74], the second largest structural component of the ECM [63]. Moreover, distinctive Brillouin frequency shift values have been reported for different parts of the human femoral head, including the measurement of trabecular bone, subchondral bone and articular cartilage. These measurements revealed a prominent mechanical heterogeneity throughout all these regions [75].

In the present study, we mapped the Brillouin elastic contrast (i.e. normalized Brillouin frequency shift) in the RZ of axolotl phalanges, which allowed us to identify distinctive mechanical properties of the cartilage ECM and embedded chondrocytes. In intact mature digits, the ECM displayed significantly higher Brillouin elastic contrast values as compared to the chondrocytes. A similar mechanical heterogeneity was observed in zebrafish larvae where ECM-rich regions displayed higher values than neighbouring cells [65]. During development, we observed gradually increasing Brillouin elastic contrast values from limb developmental stage 45 to 53. This suggests a progressive decrease in tissue compressibility as the cartilage matures, which may be explained by changes in ECM composition and structure [67]. Changes of mechanical tissue properties during cartilage development had thus far only been measured *ex vivo* [76]. By assessing tissue compressibility, we were able to observe this phenomenon for the first-time *in vivo*.

As collagen is the main component of the cartilage ECM, making up to 60% of its dry weight [63], we could perturb cartilage integrity and record a significant reduction of the Brillouin elastic contrast after treatment with collagenase *ex vivo* in a time-dependent manner. This result is in agreement with the reduction of the Brillouin frequency shift reported in porcine articular cartilage after enzymatic degradation of proteoglycans [74].

Undoubtedly, tissue mechanics play a critical role in development, and given its parallels with regeneration (reviewed in [34]), the role of mechanical tissue properties in the latter needs to be further explored. Accordingly, by successfully mapping cartilage viscoelasticity *in vivo* during development and regeneration, we detected important similarities between both processes. During development, the Brillouin elastic contrast gradually increases as the animal grows, and during regeneration, after a transient decrease, we also detected an increase in the Brillouin elastic contrast inside the cartilaginous structure. Such variations in viscoelastic cartilage properties indicate the dynamic environment, from a mechanical perspective, in which development and regeneration occur. Importantly,

development and regeneration do not only involve cartilage, but also other tissues such as muscle, blood vessels and nerves. Therefore, it will be important to assess how mechanical tissue properties are contributing to the shape of the limb from a multi-tissue perspective, integrating the information that we have for individual tissues into one integral model.

Confocal fluorescence imaging is a powerful tool to identify biologically relevant molecules or structures at the subcellular and tissue-scale levels with high resolution [77]. However, here we have demonstrated that the expression of fluorescent proteins as an indicator of tissue architecture alone may not be sufficient. During our digit regeneration experiments, by acquiring Brillouin elastic contrast maps, we show that the regenerative process was not completed mechanically by 30 days after amputation, which correlated with our regeneration progress evaluation. Contrastingly, the arrangement of SOX9 expressing cells indicated a mature-like morphology.

One major advantage of Brillouin microscopy is the possibility to access mechanical properties in a non-invasive manner, circumventing the introduction of potential artefacts caused by sample preparations prior to tissue mechanical measurements. When *in vivo* Brillouin images of the perispinal area of zebrafish larvae were compared with *ex vivo* tissue slices of the same region, differences in material properties of the sample were observed [39], indicating that sample processing for *ex vivo* measurements might introduce diverse artefacts that could affect the results. By contrast, the values for Brillouin elastic contrast in our cartilage samples *in vivo* and *ex vivo* did not change significantly (*ex vivo:* 0.0495 ± 0.0065; *in vivo:* 0.0535 ± 0.0023; $p = 0.281$ Student's *t*-test). It is important to note that in our study the positioning, i.e. the direction of the measurement, was the same for the *in vivo* and *ex vivo* samples. This, and the large distance between the measured area (digit) and the sectioning plane for tissue collection (wrist) differ from the described sample preparation between *ex vivo* and *in vivo* tissues in [39]. Tissue-specific mechanical properties may also play a contributing role [34]. The major difference between *in vivo* and *ex vivo* Brillouin frequency shift measurements in zebrafish samples were detected in muscle [39], whereas we focused on cartilage that is non-contractile and might be more resistant to rapid degradation than other tissue types. Consequently, further systematic *in vivo* and *ex vivo* measurements will be required to properly unravel how the mechanical properties of living tissues are changing not only during biologically relevant processes such as development and regeneration, but also upon certain preparatory procedures.

In regenerative biology, the axolotl is a key model organism to study limb regeneration. Its natural transparency during juvenile stages, together with the increasing availability of datasets, such as single-cell RNAseq [13,78] and the establishment of tools, such as the present work, provide new opportunities to investigate the role of tissue mechanics in regeneration. Additionally, a great body of research has been done on limb patterning and positional memory during regeneration (reviewed in [79]). The re-establishment of a complex structure such as the limb, requires the release of cells from their surrounding ECM, their de-differentiation, migration and proliferation, followed by cell differentiation and tissue patterning. These important changes are accompanied and influenced by forces produced by cell–cell and cell–ECM interactions [80,81]. Hence, confocal Brillouin microscopy opens the possibility to quantify the changes of material properties that accompany these regenerative processes and ultimately contribute to shaping the new limb.

Altogether, our work expands the potential of Brillouin microscopy as a tool to probe the *in vivo* mechanical properties of biological samples to the axolotl. With these results, we aim to set the basis for using this methodology to answer relevant questions in the field of salamander regeneration. In combination with a myriad of currently available tools, Brillouin microscopy will enable researchers to understand how mechanical tissue properties are shaping and influencing the regenerative process.

Ethics. Husbandry and experimental procedures were performed according to the Animal Ethics Committee of the State of Saxony, Germany.

Data accessibility. All custom-made softwares are available on GitHub. Image acquisition was done with BrillouinAcquisition (https://github.com/BrillouinMicroscopy/BrillouinAcquisition). Data analysis was done with BrillouinEvaluation (https://github.com/BrillouinMicroscopy/BrillouinEvaluation). Data analysis of discrete areas was done using Impose (https://github.com/GuckLab/impose).

Authors' contributions. C.R.-G.: conceptualization, data curation, formal analysis, investigation, methodology, visualization, writing—original draft and writing—review and editing; T.B.: formal analysis, investigation, methodology, resources, software, visualization and writing—review and editing; S.E.-J.: conceptualization, data curation, formal analysis, investigation, methodology, visualization, writing—original draft and writing—review and editing; R.S.: formal analysis, methodology, resources, software, validation, visualization and writing—review and editing; P.M.: methodology, resources, software and writing—review and editing; J.G.: funding acquisition, project administration, supervision and writing—review and editing; S.M.: conceptualization, project administration, supervision and writing—review and editing; T.S.-G.: conceptualization, funding acquisition, project administration, supervision, visualization, writing—original draft and writing—review and editing.

All authors gave final approval for publication and agreed to be held accountable for the work performed therein.

Conflict of interest declaration. We declare we have no competing interests.

Funding. T.S.-G. and C.R.-G. were supported by a DFG Research Grant (grant no. SA 3349/3-1). C.R.-G. was supported by the DIGS-BB fellow award. J.G. was supported by the DFG (grant no. SPP 2191—'Molecular mechanisms of functional phase separation', grant agreement number 419138906). S.E.-J. was supported by the European Union's Horizon 2020 research and innovation programme (grant agreement no. 101022810).

Acknowledgements. We would like to thank all members of the Sandoval-Guzmán Lab for continuous support and valuable feedback during the development of this work. We are also grateful to Anja Wagner, Beate Gruhl and Judith Konantz for their impeccable dedication to the axolotl care. This work was supported by the Light Microscopy Facility, a Core Facility of the CMCB Technology Platform at TU Dresden.

References

1. Bely AE, Nyberg KG. 2010 Evolution of animal regeneration: re-emergence of a field. *Trends Ecol. Evol.* **25**, 161–170. (doi:10.1016/j.tree.2009.08.005)
2. Eguchi G, Eguchi Y, Nakamura K, Yadav MC, Millán JL, Tsonis PA. 2011 Regenerative capacity in newts is not altered by repeated regeneration and ageing. *Nat. Commun.* **2**, 1–5. (doi:10.1038/ncomms1389)
3. Godwin JW, Debuque R, Salimova E, Rosenthal NA. 2017 Heart regeneration in the salamander relies on macrophage-mediated control of fibroblast activation and the extracellular landscape. *npj*

Regen. Med. **2**, 22. (doi:10.1038/s41536-017-0027-y)

4. Albors AR, Tazaki A, Rost F, Nowoshilow S, Chara O, Tanaka EM. 2015 Planar cell polarity-mediated induction of neural stem cell expansion during axolotl spinal cord regeneration. *eLife* **4**, e10230. (doi:10.7554/eLife.10230)
5. Iten LE, Bryant SV. 1976 Regeneration from different levels along the tail of the newt, *Notophthalmus viridescens*. *J. Exp. Zool.* **196**, 293–306. (doi:10.1002/jez.1401960304)
6. Iten LE, Bryant SV. 1973 Forelimb regeneration from different levels of amputation in the newt, *Notophthalmus viridescens*: length, rate, and stages. *Wilhelm Roux Arch. Entwickl Mech Org.* **173**, 263–282. (doi:10.1007/BF00575834)
7. Spallanzani L. 1768 Reproduction of the legs in the aquatic salamander. In *An essay on animal reproduction [Prodromo di un'opera da imprimersi sopra le riproduzioni animali]*, pp. 68–82. London, UK: T Becket and PA de Hondt.
8. Iismaa SE, Kaidonis X, Nicks AM, Bogush N, Kikuchi K, Naqvi N, Harvey RP, Husain A, Graham RM. 2018 Comparative regenerative mechanisms across different mammalian tissues. *npj Regen. Med.* **3**, 1–20. (doi:10.1038/s41536-018-0044-5)
9. Akash FW, Leininger E, Simkin J, Li N, Malcom CA, Sathyamoorthi S, Han M, Muneoka K. 2011 Wound healing and blastema formation in regenerating digit tips of adult mice. *Dev. Biol.* **350**, 301–310. (doi:10.1016/j.ydbio.2010.11.035)
10. Illingworth CM. 1974 Trapped fingers and amputated finger tips in children. *J. Pediatr. Surg.* **9**, 853–858. (doi:10.1016/S0022-3468(74)80220-4)
11. Stocum DL. 2017 Mechanisms of urodele limb regeneration. *Regeneration* **4**, 159–200. (doi:10.1002/reg2.92)
12. Qin T *et al.* 2021 Single-cell RNA-seq reveals novel mitochondria-related musculoskeletal cell populations during adult axolotl limb regeneration process. *Cell Death Differ.* **28**, 1110–1125. (doi:10.1038/s41418-020-00640-8)
13. Gerber T *et al.* 2018 Single-cell analysis uncovers convergence of cell identities during axolotl limb regeneration. *Science* **362**, eaaq0681. (doi:10.1126/science.aaq0681)
14. Sandoval-Guzman T *et al.* 2014 Fundamental differences in dedifferentiation and stem cell recruitment during skeletal muscle regeneration in two salamander species. *Cell Stem Cell* **14**, 174–187. (doi:10.1016/j.stem.2013.11.007)
15. Currie JD, Grosser L, Murawala P, Schuez M, Michel M, Tanaka EM, Sandoval-Guzmán T. 2019 The Prrx1 limb enhancer marks an adult subpopulation of injury-responsive dermal fibroblasts. *Biol. Open* **8**, bio043711. (doi:10.1242/bio.043711)
16. Currie JD, Kawaguchi A, Traspas RM, Schuez M, Chara O, Tanaka EM. 2016 Live imaging of axolotl digit regeneration reveals spatiotemporal choreography of diverse connective tissue progenitor pools. *Dev. Cell* **39**, 411–423. (doi:10.1016/j.devcel.2016.10.013)
17. Knapp D *et al.* 2013 Comparative transcriptional profiling of the Axolotl limb identifies a tripartite regeneration-specific gene program. *PLoS ONE* **8**, e61352. (doi:10.1371/journal.pone.0061352)
18. Wagh K, Ishikawa M, Garcia DA, Stavreva DA, Upadhyaya A, Hager GL. 2021 Mechanical regulation of transcription: recent advances. *Trends Cell Biol.* **31**, 457–472. (doi:10.1016/j.tcb.2021.02.008)
19. d'Angelo M, Benedetti E, Tupone MG, Catanesi M, Castelli V, Antonosante A, Cimini A. 2019 The role of stiffness in cell reprogramming: a potential role for biomaterials in inducing tissue regeneration. *Cells* **8**, 1036. (doi:10.3390/cells8091036)
20. De Belly H, Stubb A, Yanagida A, Labouesse C, Jones PH, Paluch EK, Chalut KJ. 2021 Membrane tension gates ERK-mediated regulation of pluripotent cell fate. *Cell Stem Cell* **28**, 273–284.e6. (doi:10.1016/j.stem.2020.10.018)
21. Weberling A, Zernicka-Goetz M. 2021 Trophectoderm mechanics direct epiblast shape upon embryo implantation. *Cell Rep.* **34**, 108655. (doi:10.1016/j.celrep.2020.108655)
22. Muncie JM, Ayad NME, Lakins JN, Xue X, Fu J, Weaver VM. 2020 Mechanical tension promotes formation of gastrulation-like nodes and patterns mesoderm specification in human embryonic stem cells. *Dev. Cell* **55**, 679–694.e11. (doi:10.1016/j.devcel.2020.10.015)
23. Nikolopoulou E, Galea GL, Rolo A, Greene NDE, Copp AJ. 2017 Neural tube closure: cellular, molecular and biomechanical mechanisms. *Development* **144**, 552–566. (doi:10.1242/dev.145904)
24. Yamamoto K *et al.* 2005 Fluid shear stress induces differentiation of Flk-1-positive embryonic stem cells into vascular endothelial cells *in vitro*. *Am. J. Physiol. Hear Physiol.* **288**, H1915–H1924. (doi:10.1152/ajpheart.00956.2004)
25. Datta N, Pham QP, Sharma U, Sikavitsas VI, Jansen JA, Mikos AG. 2006 In vitro generated extracellular matrix and fluid shear stress synergistically enhance 3D osteoblastic differentiation. *Proc. Natl Acad. Sci. USA* **103**, 2488–2493. (doi:10.1073/pnas.0505661103)
26. Brownfield DG, Venugopalan G, Lo A, Mori H, Tanner K, Fletcher DA, Bissell MJ. 2013 Patterned collagen fibers orient branching mammary epithelium through distinct signaling modules. *Curr. Biol.* **23**, 703–709. (doi:10.1016/j.cub.2013.03.032)
27. Dietrich AC, Lombardo VA, Abdelilah-Seyfried S. 2014 Blood flow and Bmp signaling control endocardial chamber morphogenesis. *Dev. Cell* **30**, 367–377. (doi:10.1016/j.devcel.2014.06.020)
28. Nelson CM, Gleghorn JP, Pang MF, Jaslove JM, Goodwin K, Varner VD, Miller E, Radisky DC, Stone HA. 2017 Microfluidic chest cavities reveal that transmural pressure controls the rate of lung development. *Development* **144**, 4328–4335. (doi:10.1242/dev.154823)
29. Segel M *et al.* 2019 Niche stiffness underlies the ageing of central nervous system progenitor cells. *Nature* **573**, 130–134. (doi:10.1038/s41586-019-1484-9)
30. Lynch B *et al.* 2017 How aging impacts skin biomechanics: a multiscale study in mice. *Sci. Rep.* **7**, 1–10. (doi:10.1038/s41598-017-13150-4)
31. Northey JJ *et al.* 2020 Stiff stroma increases breast cancer risk by inducing the oncogene ZNF217. *J. Clin. Invest.* **130**, 5721–5737. (doi:10.1172/JCI129249)
32. Bataller R, Brenner DA. 2005 Liver fibrosis. *J. Clin. Invest.* **115**, 209–218. (doi:10.1172/JCI200524282)
33. Barnes JM *et al.* 2018 A tension-mediated glycocalyx–integrin feedback loop promotes mesenchymal-like glioblastoma. *Nat. Cell Biol.* **20**, 1203–1214. (doi:10.1038/s41556-018-0183-3)
34. Vining KH, Mooney DJ. 2017 Mechanical forces direct stem cell behaviour in development and regeneration. *Nat. Rev. Mol. Cell Biol.* **18**, 728–742. (doi:10.1038/nrm.2017.108)
35. Akhtar R, Sherratt MJ, Cruickshank JK, Derby B. 2011 Characterizing the elastic properties of tissues. *Mater. Today (Kidlington)* **14**, 96–105. (doi:10.1016/S1369-7021(11)70059-1)
36. Prevedel R, Diz-Muñoz A, Ruocco G, Antonacci G. 2019 Brillouin microscopy: an emerging tool for mechanobiology. *Nat. Methods* **16**, 969–977. (doi:10.1038/s41592-019-0543-3)
37. Dil JG. 1982 Brillouin scattering in condensed matter. *Rep. Prog. Phys.* **45**, 285–334. (doi:10.1088/0034-4885/45/3/002)
38. Scarcelli G, Yun SH. 2008 Confocal Brillouin microscopy for three-dimensional mechanical imaging. *Nat. Photonics* **2**, 39–43. (doi:10.1038/nphoton.2007.250)
39. Schlüßler R *et al.* 2018 Mechanical mapping of spinal cord growth and repair in living zebrafish larvae by Brillouin imaging. *Biophys. J.* **115**, 911–923. (doi:10.1016/j.bpj.2018.07.027)
40. Schlüßler R *et al.* 2022 Correlative all-optical quantification of mass density and mechanics of sub-cellular compartments with fluorescence specificity. *eLife* **11**, e6849. (doi:10.7554/eLife.68490)
41. Scarcelli G, Polacheck WJ, Nia HT, Patel K, Grodzinsky AJ, Kamm RD, Yun SH. 2015 Noncontact three-dimensional mapping of intracellular hydromechanical properties by Brillouin microscopy. *Nat. Methods* **12**, 1132–1134. (doi:10.1038/nmeth.3616)
42. Scarcelli G, Yun SH. 2012 In vivo Brillouin optical microscopy of the human eye. *Opt. Express* **20**, 9197. (doi:10.1364/oe.20.009197)
43. Vaughan M, Randall T. 1980 Brillouin scattering, density and elastic properties of the lens and cornea of the eye. *Nature* **284**, 489–491. (doi:10.1038/284489a0)
44. Margueritat J *et al.* 2019 High-frequency mechanical properties of tumors measured by Brillouin light scattering. *Phys. Rev. Lett.* **122**, 1–6. (doi:10.1103/PhysRevLett.122.018101)
45. Conrad C, Gray KM, Stroka KM, Rizvi I, Scarcelli G. 2019 Mechanical characterization of 3D ovarian cancer nodules using brillouin confocal microscopy. *Cell Mol. Bioeng.* **12**, 215–226. (doi:10.1007/s12195-019-00570-7)
46. Mathieu V, Fukui K, Matsukawa M, Kawabe M, Vayron R, Soffer E, Anagnostou F, Haiat G. 2011 Micro-brillouin scattering measurements in mature

and newly formed bone tissue surrounding an implant. *J. Biomech. Eng.* **133**, 021006. (doi:10.1115/1.4003131)

47. Akilbekova D, Ogay V, Yakupov T, Sarsenova M, Umbayev B, Nurakhmetov A, Tazhin K, Yakovlev VV, Utegulov ZN. 2018 Brillouin spectroscopy and radiography for assessment of viscoelastic and regenerative properties of mammalian bones. *Biomed. Opt.* **23**, 097004. (doi:10.1117/1.jbo.23.9.097004)
48. Alunni Cardinali M *et al.* 2021 Brillouin–Raman microspectroscopy for the morpho-mechanical imaging of human lamellar bone. *J. R. Soc. Interface* **19**, 20210642. (doi:10.1098/rsif.2021.0642)
49. Krieg M *et al.* 2019 Atomic force microscopy-based mechanobiology. *Nat. Rev. Phys.* **1**, 41–57. (doi:10.1038/s42254-018-0001-7)
50. Harn HIC *et al.* 2021 Symmetry breaking of tissue mechanics in wound induced hair follicle regeneration of laboratory and spiny mice. *Nat. Commun.* **12**, 1–16. (doi:10.1038/s41467-021-22822-9)
51. Möllmert S, Kharlamova MA, Hoche T, Taubenberger AV, Abuhattum S, Kuscha V, Kurth T, Brand M, Guck J. 2020 Zebrafish spinal cord repair is accompanied by transient tissue stiffening. *Biophys. J.* **118**, 448–463. (doi:10.1016/j.bpj.2019.10.044)
52. Moyle LA *et al.* 2020 Three-dimensional niche stiffness synergizes with Wnt7a to modulate the extent of satellite cell symmetric self-renewal divisions. *Mol. Biol. Cell* **31**, 1703–1713. (doi:10.1091/mbc.E20-01-0078)
53. Huang TY, Wu CH, Wang MH, Chen BS, Chiou LL, Lee HS. 2015 Cooperative regulation of substrate stiffness and extracellular matrix proteins in skin wound healing of axolotls. *Biomed. Res. Int.* **2015**, 712546. (doi:10.1155/2015/712546)
54. Comellas E, Farkas JE, Kleinberg G, Lloyd K, Mueller T, Duerr TJ, Muñoz JJ, Monaghan JR, Shefelbine SJ. 2022 Local mechanical stimuli shape tissue growth in vertebrate joint morphogenesis. *Proc. R. Soc. B* **289**, 20220621. (doi:10.1098/rspb.2022.0621)
55. Kozhemyakina E, Lassar AB, Zelzer E. 2015 A pathway to bone: signaling molecules and transcription factors involved in chondrocyte development and maturation. *Development* **142**, 817–831. (doi:10.1242/dev.105536)
56. Riquelme-Guzmán C, Schuez M, Böhm A, Knapp D, Edwards-Jorquera S, Ceccarelli AS, Chara O, Rauner M, Sandoval-Guzmán T. 2021 Postembryonic development and aging of the appendicular skeleton in Ambystoma mexicanum. *Dev. Dyn.* **251**, 1015–1034. (doi:10.1002/dvdy.407)
57. Sobkow L, Epperlein HH, Herklotz S, Straube WL, Tanaka EM. 2006 A germline GFP transgenic axolotl and its use to track cell fate: dual origin of the fin mesenchyme during development and the fate of blood cells during regeneration. *Dev. Biol.* **290**, 386–397. (doi:10.1016/j.ydbio.2005.11.037)
58. Antonacci G *et al.* 2020 Recent progress and current opinions in Brillouin microscopy for life science applications. *Biophys. Rev.* **12**, 615–624. (doi:10.1007/s12551-020-00701-9)
59. Purushothaman S, Elewa A, Seifert AW. 2019 Fgf-signaling is compartmentalized within the mesenchyme and controls proliferation during salamander limb development. *eLife* **8**, e48507. (doi:10.7554/eLife.48507)
60. Nye HLD, Cameron JA, Chernoff EAG, Stocum DL. 2003 Extending the table of stages of normal development of the axolotl: limb development. *Dev. Dyn.* **226**, 555–560. (doi:10.1002/dvdy.10237)
61. Schindelin J *et al.* 2012 Fiji: an open-source platform for biological-image analysis. *Nat. Methods* **9**, 676–682. (doi:10.1038/nmeth.2019)
62. Tomczak M, Tomczak E. 2014 The need to report effect size estimates revisited. An overview of some recommended measures of effect size. *Trends Sport Sci.* **1**, 19–25.
63. Fox AJS, Bedi A, Rodeo SA. 2009 The basic science of articular cartilage: structure, composition, and function. *Sports Health* **1**, 461–468. (doi:10.1177/1941738109350438)
64. Hutchison C, Pilote M, Roy S. 2007 The axolotl limb: a model for bone development, regeneration and fracture healing. *Bone* **40**, 45–56. (doi:10.1016/j.bone.2006.07.005)
65. Bevilacqua C, Sánchez-Iranzo H, Richter D, Diz-Muñoz A, Prevedel R. 2019 Imaging mechanical properties of sub-micron ECM in live zebrafish using Brillouin microscopy. *Biomed. Opt. Express* **10**, 1420–1431. (doi:10.1364/boe.10.001420)
66. Maloney JM, Nikova D, Lautenschläger F, Clarke E, Langer R, Guck J, Van Vliet KJ. 2010 Mesenchymal stem cell mechanics from the attached to the suspended state. *Biophys. J.* **99**, 2479–2487. (doi:10.1016/j.bpj.2010.08.052)
67. Fowler DA, Larsson HCE. 2020 The tissues and regulatory pattern of limb chondrogenesis. *Dev. Biol.* **463**, 124–134. (doi:10.1016/j.ydbio.2020.04.009)
68. Amini R, Bhatnagar A, Schlüßler R, Möllmert S, Guck J, Norden C. 2022 Amoeboid-like neuronal migration ensures correct horizontal cell layer formation in the developing vertebrate retina. *eLife* **11**, e76408. (doi:10.7554/eLife.76408)
69. Young JL, Holle AW, Spatz JP. 2016 Nanoscale and mechanical properties of the physiological cell-ECM microenvironment. *Exp. Cell Res.* **343**, 3–6. (doi:10.1016/j.yexcr.2015.10.037)
70. Harley R, James D, Miller A, White JW. 1977 Phonons and the elastic moduli of collagen and muscle [38]. *Nature* **267**, 285–287. (doi:10.1038/267285a0)
71. Cusack S, Miller A. 1979 Determination of the elastic constants of collagen by Brillouin light scattering. *J. Mol. Biol.* **135**, 39–51. (doi:10.1016/0022-2836(79)90339-5)
72. Cusack S, Lees S. 1984 Variation of longitudinal acoustic velocity at gigahertz frequencies with water content in rat-tail tendon fibers. *Biopolymers* **23**, 337–351. (doi:10.1002/bip.360230212)
73. Palombo F, Winlove CP, Edginton RS, Green E, Stone N, Caponi S, Madami M, Fioretto D. 2014 Biomechanics of fibrous proteins of the extracellular matrix studied by Brillouin scattering. *J. R. Soc. Interface* **11**, 20140739. (doi:10.1098/rsif.2014.0739)
74. Wu PJ, Masouleh MI, Dini D, Paterson C, Török P, Overby DR, Kabakova IV. 2019 Detection of proteoglycan loss from articular cartilage using Brillouin microscopy, with applications to osteoarthritis. *Biomed. Opt. Express* **10**, 2457–2466. (doi:10.1364/boe.10.002457)
75. Cardinali MA, Dallari D, Govoni M, Stagni C, Marmi F, Tschon M, Brogini S, Fioretto D, Morresi A. 2019 Brillouin micro-spectroscopy of subchondral, trabecular bone and articular cartilage of the human femoral head. *Biomed. Opt. Express.* **10**, 2606. (doi:10.1364/boe.10.002606)
76. Gannon AR, Nagel T, Bell AP, Avery NC, Kelly DJ. 2015 Postnatal changes to the mechanical properties of articular cartilage are driven by the evolution of its collagen network. *Eur. Cells Mater.* **29**, 105–123. (doi:10.22203/eCM.v029a09)
77. Elliott AD. 2020 Confocal microscopy: principles and modern practices. *Curr. Protoc. Cytom.* **92**, e68. (doi:10.1002/cpcy.68))
78. Leigh ND *et al.* 2018 Transcriptomic landscape of the blastema niche in regenerating adult axolotl limbs at single-cell resolution. *Nat. Commun.* **9**, 5153. (doi:10.1038/s41467-018-07604-0)
79. Otsuki L, Tanaka EM. In press. Positional memory in vertebrate regeneration: a century's insights from the salamander limb. *Cold Spring. Harb. Perspect. Biol.* a040899. (doi:10.1101/cshperspect.a040899)
80. Petreaca M, Martins-Green M. 2019 Cell–extracellular matrix interactions in repair and regeneration. In: *Principles of regenerative medicine* (eds A Atala, R Lanza, T Mikos, R Nerem), pp. 15–35. Amsterdam, The Netherlands: Elsevier.
81. Boilly B, Lheureux E, Boilly-Marer Y, Bart A. 1990 Cell interactions and regeneration control. *Int. J. Dev. Biol.* **34**, 219–231. (doi:10.1387/ijdb.2203459)